Composite Structures 331 (2024) 117876

Contents lists available at ScienceDirect

Composite Structures

journal homepage: www.elsevier.com/locate/compstruct

A quasi-3D hyperbolic formulation for the buckling study of metal foam microplates layered with graphene nanoplatelets-embedded nanocomposite patches with temperature fluctuations

Saeid Zavari [a], Ali Kaveh [a], Hossein Babaei [b], Ehsan Arshid [c], Rossana Dimitri [d], Francesco Tornabene [d,*]

[a] Department of Mechanical and Industrial Engineering, Louisiana State University, Baton Rouge, LA 70803, USA
[b] Department of Civil and Environmental Engineering, Louisiana State University, Baton Rouge, LA 70803, USA
[c] Advanced Research and Development Center, LIPS Research Foundation, European International University, Paris, France
[d] Department of Innovation Engineering, University of Salento, 73100, Lecce, Italy

ARTICLE INFO

Keywords:
Buckling analysis
Metal foams
Graphene nanoplatelets
Thermal environment
Quasi-3D shear and normal deformation theory
Microplates

ABSTRACT

The work analyzes the buckling behavior of size-dependent microplates with a metal foam core, covered by graphene nanoplatelets (GNPs)-embedded nanocomposite patches. Microplates rest on a bi-parameter elastic substrate, and they are immersed in a thermal environment to observe the effect of temperature fluctuations on their elastic buckling performance. All material properties for each layer of the microstructure are thickness-dependent. A novel quasi-3D shear and normal (Q-3D S-N) hyperbolic theory is here proposed to describe the kinematic relations, accounting for the transverse normal strain. At the same time, a modified couple stress theory (MCST) is employed to account for the size dependence of the mechanical behavior due to the presence of a material length-scale parameter. Using the energy method and virtual work principle, the differential equilibrium equations are derived and solved analytically, where solutions are verified against the existing literature. The study focuses on the impact of different parameters on the normalized critical buckling load (NCBL). Based on the results from the systematic investigation, it is found that the addition of GNPs to the microplate enhances its stiffness, leading to increased values of NCBL, which in turn reduce for an increased imperfection ratio.

1. Introduction

In the field of structural mechanics, understanding the behavior of beam, plate, and shell structural members under various loading conditions is of paramount importance. To accurately analyze the mechanical performances of these structures, engineers and researchers have developed different shear deformation theories that account for the influence of shear deformations. Among many, one advanced theory that has shown promising advantages over traditional approaches is the quasi-3D shear and normal (Q-3D S-N) deformation theory. Shear deformation theories go beyond the classical theory, which assumes that cross-sectional planes remain normal to the mid-surface and neglect the effects of shear deformation. These theories are applicable to thick-walled structures, where the relative significance of shear deformations becomes more pronounced. The Q-3D S-N theory is a refined theory that bridges the gap between 2D and fully 3D approaches. Unlike traditional theories, which often require complex and computationally expensive 3D finite element models, the Q-3D S-N theory provides a more efficient and accurate alternative. More specifically, the Q-3D S-N theory considers the parabolic distribution of transverse shear stresses through the thickness of the structure. This allows for more accurate predictions of shear stress and strain fields, especially in thick structures where shear deformation effects become significant. Also, the quasi-3D approach significantly reduces the number of degrees of freedom, compared to fully 3D models, resulting in faster and more computationally efficient analyses, while ensuring a high level of accuracy. The Q-3D S-N theory is particularly well-suited for analyzing plates and shells, as it incorporates both the advantages of higher-order theories and the computational efficiency of lower-order models. This theory is versatile and applicable to a wide range of loading conditions, including static, dynamic, and thermal loads, making it valuable for different engineering disciplines. Furthermore, Q-3D S-N theory has shown a

* Corresponding author.
E-mail address: francesco.tornabene@unisalento.it (F. Tornabene).

https://doi.org/10.1016/j.compstruct.2024.117876
Received 29 October 2023; Received in revised form 6 December 2023; Accepted 2 January 2024
Available online 11 January 2024

superior accuracy in predicting the buckling and vibration behavior of beams, plates, and shells, enabling engineers to design more robust and reliable structures [1–3]. As technology and computational capabilities continue to evolve, the use of such advanced shear deformation theories is expected to become even more prevalent in the design and analysis of complex structures.

Metal foams are a class of lightweight materials with a unique cellular structure, characterized by a three-dimensional network of gas-filled voids or pores within a solid metal matrix [4]. This cellular structure imparts several advantageous properties to metal foams, making them suitable for a wide range of applications. Metal foams have excellent energy absorption capabilities due to their cellular structure. They are used in automotive components, crash barriers, and protective gear to enhance safety during impacts and collisions. Certain metal foams, especially closed-cell foams, can be used as lightweight and high-strength structural components in aerospace, automotive, and construction industries. Open-cell metal foams with high thermal conductivity are used in heat exchangers, electronic cooling, and thermal management systems to dissipate heat efficiently [5–9].

Nanocomposites are materials composed of a matrix (polymer, metal, ceramic, etc.) reinforced with nanoscale fillers or reinforcements. These nano-scale fillers can be nanoparticles, nanofibers, or nanosheets. The addition of these nano reinforcements imparts exceptional mechanical, electrical, thermal, and barrier properties to the composite material compared to conventional composites. Nanocomposite structures, primarily those reinforced with graphene nanoplatelets (GNPs), represent a class of advanced materials with remarkable properties owing to their unique composition. Graphene is a two-dimensional sheet of carbon atoms arranged in a honeycomb lattice. When these graphene sheets are stacked together to form a platelet-like structure, they are referred to as GNPs. GNPs are thin, lightweight, and possess an outstanding mechanical strength, electrical conductivity, and thermal conductivity, making them ideal candidates for reinforcing composite materials. GNP-reinforced nanocomposite structures offer a wide range of applications due to their exceptional properties. As research continues to advance in the field of nanotechnology, these composites are expected to play an increasingly significant role in various industries, paving the way for innovative and high-performance materials [10–14].

Microstructures refer to small-scale features, patterns, or arrangements of materials that are typically measured on a micron or submicron scale. These microscale features have unique properties and play a crucial role in determining the overall behavior and performance of materials. The applications of microstructures are vast and diverse, encompassing various fields of science, engineering, and technology. Microstructures are fundamental to the design and fabrication of microelectronic devices, integrated circuits, and microprocessors. These structures, such as transistors, capacitors, and interconnects, form the building blocks of modern electronic devices. Microelectromechanical systems devices are microstructures that combine electrical and mechanical components on a single chip. They find applications in sensors, actuators, accelerometers, gyroscopes, microphones, and microfluidic devices, among others. Microstructures are used in optical devices and photonics applications, such as diffractive optical elements, micro lenses, photonic crystals, and integrated photonics circuits. In nanotechnology, microstructures are used as templates to create nanostructures and nanomaterials. They form the foundation for many nanoscale devices and applications. Microstructures are also employed in aerospace and automotive applications for lightweight materials, high-performance alloys, and improved mechanical properties [15–18].

Now, it turns to provide a brief literature review about related published works in recent years. Jabbari et al. [19] conducted a study on the buckling behavior of a solid circular plate with porosity, which was encased with piezoelectric actuators. Their research revealed that as the porosity increased, the critical buckling load (CBL) decreased. Subsequently, Mojahedin et al. [20] examined the mechanical buckling of functionally graded (FG) circular plates made of porous material, using a higher-order shear deformation theory. Their investigation considered various parameters effects on the CBLs, assuming the plate to be saturated with fluid. Similarly, Feyzi and Khorshidvand [21] conducted a comparable study on the post-buckling behavior of porous circular plates subjected to a mechanical loading. They presented two distinct scenarios, for a given load and deflection, respectively. The governing equations were numerically solved using the shooting method with a Newton iteration. Dhuria et al. [22] discussed the impact of porosity distribution on the static and buckling response of porous FG plates with simply supported edges and employed an inverse hyperbolic shear deformation theory as a higher-order approach to obtain their results. Van Vinh et al. [23] introduced an innovative mixed four-node quadrilateral plate element based on an improved first-order shear deformation theory, which eliminated the requirement of shear correction factor. This element was adopted to analyze the bending and buckling behavior of bi-directional FG plates with porosity. Many further works in literature have focused on the mechanical performance of structures made of porous materials [24–30]. Cuong Le et al. [31] conducted a research on small-scale structures and explored the linear and nonlinear response of a microplate made from porous metal foam. They used the modified couple stress theory (MCST) in conjunction with the isogeometric analysis for their investigation. Pham and Nguyen [32] studied the dynamic stability characteristics of a porous FG microplate. The microplate was subjected to periodic uni-axial/bi-axial in-plane compressions, where a refined plate theory was combined with MCST within an isogeometric analysis framework. Hung et al. [33] performed a refined isogeometric plate analysis of porous metal foam microplates using the modified strain gradient theory, and considered the influence of various parameters on results. At the same time, Tran et al. [34] introduced a novel approach that combined artificial neural networks and balancing composite motion optimization. This method was developed to address optimization problems and predict stochastic vibration and buckling behaviors of FG porous microplates, considering uncertainties in material properties. Among many other notable contributions in the field of microstructures, the studies in Ref. [35–43] cover various aspects of microstructural analysis, design, and optimization within the engineering domain. In the field of reinforced composites, several studies can be found in the open literature. For example, Chen et al. [44] investigated a novel porous FG composite model reinforced with GNPs. They analyzed the thermo-mechanical buckling and post-buckling responses of this composite. In their study, the Young modulus, the shear modulus, as well as the Poisson's ratio of the porous matrix, were all functions of the porosity coefficient. On a related note, Fang et al. [45] used the MCST in their research to examine the thermal buckling and vibration behavior of rotating porous FG GNPs-reinforced microplates. The study was based on the higher-order shear deformation theory, which allowed for a comprehensive analysis of these composite microplates under thermal loading conditions. Anamagh and Bediz [46] conducted a study on the free vibration and buckling behavior of FG porous plates reinforced by GNPs. They employed the spectral Chebyshev approach to analyze the plates response. Yaghoobi and Taheri [47] provided an analytical solution for the buckling capacity of sandwich plates with a porous core reinforced with GNPs. Their study focused on the critical buckling load of such composite plates. In a separate work, Kim et al. [48] analyzed the bending, free vibration, and buckling performances of microplates made from MCST-based FG porous material with simply supports. In recent years, Khorasani et al. [49] have adopted a Q-3D theory to enhance the accuracy for the study of the thermo-elastic buckling performance of honeycomb sandwich plates. This advanced computational approach allowed for a more detailed and accurate analysis of the buckling behavior under thermal loading conditions. Other related studies on similar topics can be found in [50–54] focusing on various aspects of the mechanical performance of sandwich microplates, possibly employing different numerical or analytical methods to investigate their response under various conditions.

In absence of works focusing on the elastic buckling behavior of sandwich microplates with a mid-layer made from metal foams and faces from FG GNPs-reinforced nanocomposites, the present study offers novel significant and useful insights in this field, with potential applications to solar cells, temperature sensors or strain sensors for structural health monitoring, as small-scale electro-mechanical systems. The combination of metal foams as mid-layer and FG GNPs-reinforced nanocomposites as faces is a novel way to yield unique mechanical and thermal properties, while considering composite microplates under various loading conditions. The use of Q-3D S-N theory based on a hyperbolic function, which considers the transverse normal strain without any shear correction factor, enhances the accuracy and novelty of the analysis compared to simpler 2D higher-order shear deformation theories. Furthermore, the employment of the MCST enables the consideration of scale influence, which is crucial in analyzing small-scale structures. Setting the material length-scale parameter to zero allows conversion to classical elasticity theory (CET) for comparison and validation purposes. Deriving differential equilibrium equations and solving them analytically further distinguishes this study, allows for a precise evaluation of the buckling behavior. The investigation of various parameters and their effect on the CBLs offer valuable insights in terms of mechanical performances of these unique composite microplates, with important consequences for optimization design purposes of sandwich microstructural components in engineering applications.

2. Model's description and materials properties

Let consider a three-layered microplate, as shown in Fig. 1, which is made of a metal foam core with thickness h_c and two FG-GNPs-reinforced composite face sheets with thickness h_t and h_b at the top and bottom layers, respectively, for a total thickness h. The reference Cartesian coordinate system is located at the mid-plane of the sandwich microstructure, with length a in the $x-$ direction, width b in the $y-$ direction, and thickness h in the $z-$ direction.

In this work, we employ a Q-3D S-N theory, which considers the transverse normal strain effect along with inverse tangential variation of in-plane displacements across the microplate thickness. The present model satisfies both non-linear variation and zero transverse shear stresses across the microplate thickness. Based on the Q-3D S-N deformation theory, the displacement field at any random position of the microplate is defined as [1]

$$U(x,y,z) = u(x,y) - z\frac{\partial w_b}{\partial x}(x,y) - f(z)\frac{\partial w_s}{\partial x}(x,y),$$

$$V(x,y,z) = v(x,y) - z\frac{\partial w_b}{\partial y}(x,y) - f(z)\frac{\partial w_s}{\partial y}(x,y),$$

$$W(x,y,z) = w_b(x,y) - w_s(x,y) - h(z)\beta(x,y) \tag{1}$$

where the kinematic components u and v refer to the x and y directions, respectively. In addition, w_s and w_b stand for the transverse shear and bending displacements resulting from stretching. Moreover, the symbol β represents an additional component that takes into account the effect of normal stress in the displacement field. In the context of the Q-3D S-N theory, functions $f(z)$ and $h(z)$ represent the transverse displacement and the through-thickness displacement variation, respectively. These functions are used to account for higher-order effects in the displacement field, allowing for more accurate modeling of the bending and shear behavior in composite and sandwich structures and they are defined based on a hyperbolic form as below

$$f(z) = \frac{h\sinh(\pi z/h) - z}{\pi\cosh(\pi/2) - 1}, h(z) = 1 - f'(z) \tag{2}$$

where $f'(z)$ indicates the differentiation of the function with respect to z. Next, the strain field can be obtained in terms of kinematic components as

$$\varepsilon_{xx} = \frac{\partial u(x,y)}{\partial x} - z\frac{\partial^2 w_b(x,y)}{\partial x^2} - f(z)\frac{\partial^2 w_s(x,y)}{\partial x^2},$$

$$\varepsilon_{yy} = \frac{\partial v(x,y)}{\partial y} - z\frac{\partial^2 w_b(x,y)}{\partial y^2} - f(z)\frac{\partial^2 w_s(x,y)}{\partial y^2},$$

$$\varepsilon_{zz} = h'(z)\beta(x,y),$$

$$\gamma_{xy} = \frac{\partial u(x,y)}{\partial y} + \frac{\partial v(x,y)}{\partial x} - 2z\frac{\partial^2 w_b(x,y)}{\partial y \partial x} - 2f(z)\frac{\partial^2 w_s(x,y)}{\partial y \partial x},$$

$$\gamma_{xz} = h(z)\left(\frac{\partial \beta(x,y)}{\partial x} + \frac{\partial w_s(x,y)}{\partial x}\right),$$

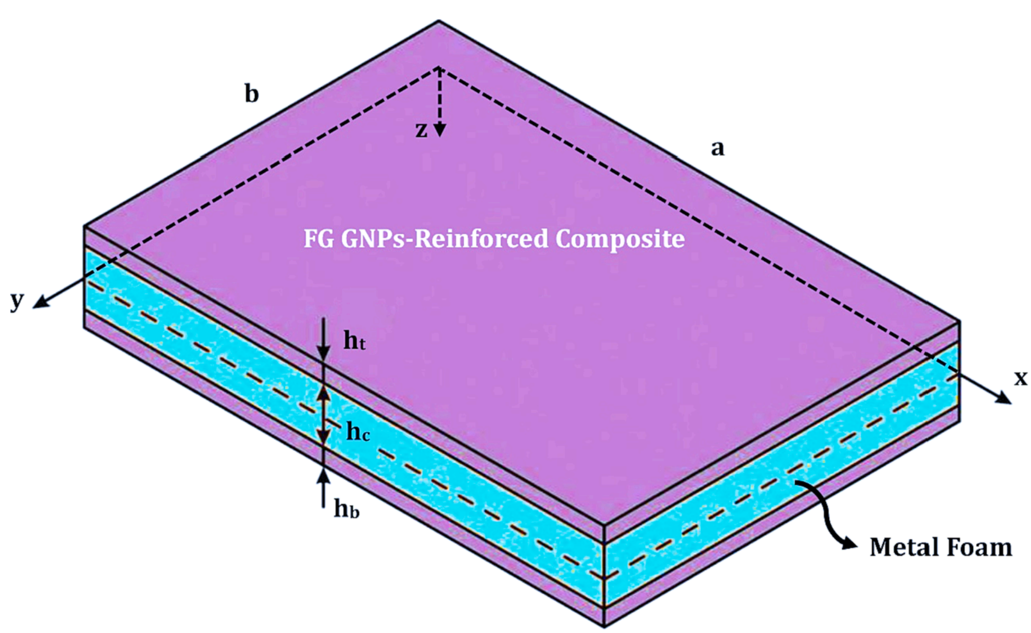

Fig. 1. Arrangement of the metal foam microplate coated by FG GNPs-reinforced composite faces.

$$\gamma_{yz} = h(z)\left(\frac{\partial\beta(x,y)}{\partial y} + \frac{\partial w_s(x,y)}{\partial y}\right) \tag{3}$$

Now, the constitutive law for the core and face sheets will account for the thermal environment as follows [55]

$$\sigma_{ij}^{c,f} = Q_{ijkl}^{c,f}(\varepsilon_{kl} - \alpha_{ij}^{c,f}\Delta T) \tag{4}$$

whose parameters Q, α, and ΔT are associated with the stiffness components, thermal expansion coefficient, and temperature differences, respectively, whereas superscripts c and f refer to the core and face sheets of the microstructure, respectively. The stiffness components for all three layers based on Q-3D S-N theory can be denoted as follows [56]:

$$Q_{ii}^{c,f} = \frac{(1-\nu_{c,f})E_{c,f}(z)}{(1-2\nu_{c,f})(1+\nu_{c,f})}, (i = 1,2,3) \tag{5}$$

$$Q_{jj}^{c,f} = \frac{E_{c,f}(z)}{2(1+\nu_{c,f})}, (j = 4,5,6)$$

$$Q_{12}^{c,f} = Q_{13}^{c,f} = Q_{23}^{c,f} = \frac{\nu_{c,f}E_{c,f}(z)}{(1-2\nu_{c,f})(1+\nu_{c,f})}$$

As stated hitherto, in the current model, we consider a metal foam core to yield a light structure, such that $E_c(z)$ represents the elastic modulus, and ν_c refers the Poisson's ratio of the core. For the sake of simplicity, ν_c is assumed to be constant and does not vary along the core thickness. However, the variation of the elastic constants are primarily affected by the type of core imperfection distribution. In case of "Type A" imperfection, with a uniform distribution of the imperfection in the core, the elastic modulus and density are independent of the thickness parameter and can be defined as [57]

$$E_c = E_0 - E_0\left[1 - \left(\frac{2\sqrt{1-\gamma}-2}{\pi+1}\right)^2\right], \tag{6a}$$

$$\rho_c = \rho_0\sqrt{1 - \left[1 - \left(\frac{2\sqrt{1-\gamma}-2}{\pi+1}\right)^2\right]}, \tag{6b}$$

$$\alpha_c = \alpha_0\sqrt{1 - \left[1 - \left(\frac{2\sqrt{1-\gamma}-2}{\pi+1}\right)^2\right]}, \tag{6c}$$

The imperfection ratio, γ, is defined as the ratio of the volume of pores to the total volume of the material. For a "Type B" configuration, instead, the core layer exhibits a symmetrical distribution of imperfection, such that the elastic modulus and density variations in the core obey the following rules [58]

$$E_c(z) = E_0 - E_0\gamma\cos\left(\frac{\pi z}{h_c}\right), \tag{7a}$$

$$\rho_c(z) = \rho_0 - \rho_0\left[1 - \sqrt{1-\gamma}\right]\cos\left(\frac{\pi z}{h_c}\right), \tag{7b}$$

$$\alpha_c(z) = \alpha_0 - \alpha_0\left[1 - \sqrt{1-\gamma}\right]\cos\left(\frac{\pi z}{h_c}\right), \tag{7c}$$

A "Type C" imperfection involves a non-symmetric arrangement of pores throughout the core layer. The basic properties can be characterized as follows [59]

$$E_c(z) = E_0 - E_0\gamma\cos\left(\frac{\pi z}{2h_c} + \frac{\pi}{4}\right), \tag{8a}$$

$$\rho_c(z) = \rho_0 - \rho_0\left[1 - \sqrt{1-\gamma}\right]\cos\left(\frac{\pi z}{2h_c} + \frac{\pi}{4}\right), \tag{8b}$$

$$\alpha_c(z) = \alpha_0 - \alpha_0\left[1 - \sqrt{1-\gamma}\right]\cos\left(\frac{\pi z}{2h_c} + \frac{\pi}{4}\right) \tag{8c}$$

As far as the face sheets of the microstructure is concerned, they consist of a matrix phase and GNPs reinforcement, with constitutive laws as already defined in Eq. (4), and stiffness components as introduced in Eq. (5), but with different definitions.

More specifically, the Young's modulus of the faces is defined as [60]

$$E_f(z) = \frac{E_m}{8}(3\beta_l + 5\beta_w), \tag{9}$$

where E_m describes the stiffness of the matrix phase in the microstructure. It is also [61]

$$\beta_l = \frac{1+\xi_l^{GNPs}\eta_l^{GNPs}V_{GNPs}}{1-\eta_l^{GNPs}V_{GNPs}}, \beta_w = \frac{1+\xi_w^{GNPs}\eta_w^{GNPs}V_{GNPs}}{1-\eta_w^{GNPs}V_{GNPs}}, \tag{10}$$

where the parameters ξ_l^{GNPs} and ξ_w^{GNPs} are related to the geometric properties of GNPs, while η_l^{GNPs} and η_w^{GNPs} are related to their material properties. Such parameters depend on the specific properties of the GNPs being used in the microstructure, i.e.

$$\xi_l^{GNPs} = \frac{2l_{GNPs}}{t_{GNPs}}, \xi_w^{GNPs} = \frac{2w_{GNPs}}{t_{GNPs}} \tag{11}$$

$$\eta_l^{GNPs} = \frac{\left(\frac{E_{GNPs}}{E_m}\right) - 1}{\left(\frac{E_{GNPs}}{E_m}\right) + \xi_l^{GNPs}}, \eta_w^{GNPs} = \frac{\left(\frac{E_{GNPs}}{E_m}\right) - 1}{\left(\frac{E_{GNPs}}{E_m}\right) + \xi_w^{GNPs}}$$

In Eq. (11), the length, thickness, and width of the GNPs are represented by l_{GNPs}, t_{GNPs}, and w_{GNPs}, respectively. The properties of the GNPs are further regulated using the extended rule of mixture [62], i.e.

$$\begin{Bmatrix}\rho_f(z)\\ \nu_f(z)\end{Bmatrix} = \begin{Bmatrix}\rho_{GNPs}\\ \nu_{GNPs}\end{Bmatrix}V_{GNP} + \begin{Bmatrix}\rho_m\\ \nu_m\end{Bmatrix}V_m, \alpha_f(z) = \frac{V_{GNPs}E_{GNPs}\alpha_{GNPs} + V_mE_m\alpha_m}{V_{GNPs}E_{GNPs} + V_mE_m}, \tag{12}$$

V_{GNPs} and V_m being the volume fractions of GNPs and matrix, respectively, whose sum must be equal to one, as they fully account for the overall volume of the microstructure. Hereafter, we assume five different GNPs dispersions in the z-direction, defined as follows, in terms of their total mass fraction, g^*_{GNPs} [63]

$$V_{GNPs}(z) = \begin{cases} g^*_{GNPs} & \text{Uniform}\\ \left[1 - \frac{2z}{h_f}\right]g^*_{GNPs} & \text{FG-}A\\ \left[1 + \frac{2z}{h_f}\right]g^*_{GNPs} & \text{FG-}V\\ 2\left[1 - \frac{2z}{h_f}\right]g^*_{GNPs} & \text{FG-}O\\ \left[\frac{4|z|}{h_f}\right]g^*_{GNPs} & \text{FG-}X \end{cases} \tag{13}$$

with h_f the faces thickness.

3. Equilibrium equations

By employing the energy method formulation, the equilibrium equations can be obtained from the following relation [64]:

$$\delta(U_s - W_e) = 0 \tag{14}$$

in which U_s is the strain energy and W_e is the external work applied on the sandwich microstructure. The strain energy of the system is the sum of the two contributions associated to the face sheets and the metal foam core, i.e.

$$U_s^T = U_s^c + U_s^f \tag{15}$$

Note also that a MCST is employed to incorporate small-scale effects. The MCST-based strain energy can be expressed using the aforementioned theory as presented below [65]

$$U_s^T = \frac{1}{2}\int_x\int_y\int_{-h/2}^{+h/2}\left[\sigma_{ij}^{c,f}\varepsilon_{ij} + m_{ij}^{c,f}\chi_{ij}\right]\,\mathrm{d}z\,\mathrm{d}y\,\mathrm{d}x(i,j=x,y,z) \tag{16}$$

where m_{ij} and χ_{ij} refer to the stress and symmetric curvature tensors, respectively. Another important aspect is that m_{ij} is a component of the couple stress tensor, which plays a crucial role at a micro and nano-scale level, when small-scale effects become significant for an accurate mechanical modeling. More specifically, m_{ij} and χ_{ij} are related as

$$m_{ij}^{c,f} = 2\,l^2\mu(z)\chi_{ij}\ , \tag{17}$$

where l represents the material length-scale parameter of MCST, and $\mu(z)$ denotes the Lame's parameter defined as $\mu(z) = \frac{E(z)}{2(1+\nu)}$. Also, the symmetric curvature components are defined as

$$\chi_{xx} = \frac{\partial\omega_x}{\partial x}, \chi_{yy} = \frac{\partial\omega_y}{\partial y}, \chi_{zz} = \frac{\partial\omega_z}{\partial z}, \tag{18}$$

$$2\chi_{yz} = \frac{\partial\omega_z}{\partial y} + \frac{\partial\omega_y}{\partial z}, 2\chi_{xz} = \frac{\partial\omega_z}{\partial x} + \frac{\partial\omega_x}{\partial z}, 2\chi_{xy} = \frac{\partial\omega_y}{\partial x} + \frac{\partial\omega_x}{\partial y}$$

where ω_i represents the infinitesimal rotation vector in the i direction, such that

$$2\omega_x = \frac{\partial W}{\partial y} - \frac{\partial V}{\partial z}, 2\omega_y = \frac{\partial U}{\partial z} - \frac{\partial W}{\partial x}, 2\omega_z = \frac{\partial V}{\partial x} - \frac{\partial U}{\partial y} \tag{19}$$

A bi-parameter Pasternak type substrate is considered as support for our sandwich microplate, which contributes to the following external work [66]

$$W_e^{Sub} = \frac{1}{2}\int_A\left(-K_w(w_b+w_s)^2 + K_p(w_b+w_s)\left(\frac{\partial^2(w_b+w_s)}{\partial x^2} + \frac{\partial^2(w_b+w_s)}{\partial y^2}\right)\right)dA \tag{20}$$

where K_w is the Winkler spring coefficient and K_p is the shear layer parameter.

The thermal environment work can be expressed as follows [67]

$$W_e^{Thermal} = \frac{1}{2}\int_A\left(N_x^T\left(\frac{\partial(w_b+w_s)}{\partial x}\right)^2 + N_y^T\left(\frac{\partial(w_b+w_s)}{\partial y}\right)^2\right)dA \tag{21}$$

where the thermal load in the x and y directions is defined as

$$N_x^T = \int_{-h/2}^{+h/2}\left[Q_{11}^{c,f} + Q_{12}^{c,f} + Q_{13}^{c,f}\right]\alpha^{c,f}\Delta T\,\mathrm{d}z, \tag{22}$$

$$N_y^T = \int_{-h/2}^{+h/2}\left[Q_{21}^{c,f} + Q_{22}^{c,f} + Q_{23}^{c,f}\right]\alpha^{c,f}\Delta T\,\mathrm{d}z$$

The mechanical contribution due to the in-plane forces N_x^M and N_y^M in the x and y directions, is defined as

$$W_e^{Mech} = \frac{1}{2}\int_A\left(N_x^M\left(\frac{\partial(w_b+w_s)}{\partial x}\right)^2 + N_y^M\left(\frac{\partial(w_b+w_s)}{\partial y}\right)^2\right)dA \tag{23}$$

These loads are defined as $\varkappa_x N_x$ and $\varkappa_y N_y$, by means of magnitudes $\varkappa_x$ and $\varkappa_y$, respectively. In a bi-axial buckling scenario, both $\varkappa_x$ and $\varkappa_y$ assume a non-null value, differently from the uniaxial case where one of them is ignored.

The overall external work is, thus, determined as

$$W_e = W_e^{Sub} + W_e^{Thermal} + W_e^{Mech} \tag{24}$$

By substituting Eqs. (16) and (24) into Eq. (14), we obtain the governing equilibrium equations of the problem, by assuming, in turn, a null value for coefficients δu, δv, δw_b, δw_s, and $\delta\beta$, namely

δu :

$$Q_{111}\frac{\partial^3 w_b}{\partial x^3} - Q_{110}\frac{\partial^2 u}{\partial x^2} + Q_{113}\frac{\partial^3 w_s}{\partial x^3} - Q_{120}\frac{\partial^2 v}{\partial x\partial y} + Q_{121}\frac{\partial^3 w_b}{\partial x\partial y^2} + Q_{123}\frac{\partial^3 w_s}{\partial x\partial y^2} - Q_{660}\frac{\partial^2 v}{\partial x\partial y} - Q_{136}\frac{\partial\beta}{\partial x}$$
$$-Q_{660}\frac{\partial^2 u}{\partial y^2} + 2\left(Q_{661}\frac{\partial^3 w_b}{\partial x\partial y^2} + Q_{663}\frac{\partial^3 w_s}{\partial x\partial y^2}\right) + \frac{K_0}{4}\left(\frac{\partial^4 u}{\partial y^4} - \frac{\partial^4 v}{\partial x\partial y^3} - \frac{\partial^4 v}{\partial x^3\partial y} + \frac{\partial^4 u}{\partial x^2\partial y^2}\right) = 0, \tag{25}$$

δv :

$$Q_{121}\frac{\partial^3 w_b}{\partial x^2\partial y} - Q_{120}\frac{\partial^2 u}{\partial x\partial y} + Q_{123}\frac{\partial^3 w_s}{\partial x^2\partial y} - Q_{220}\frac{\partial^2 v}{\partial y^2} + Q_{221}\frac{\partial^3 w_b}{\partial y^3} + Q_{223}\frac{\partial^3 w_s}{\partial y^3} - Q_{660}\frac{\partial^2 v}{\partial x^2} - Q_{236}\frac{\partial\beta}{\partial y}$$
$$-Q_{660}\frac{\partial^2 u}{\partial y\partial x} + 2\left(Q_{661}\frac{\partial^3 w_b}{\partial x^2\partial y} + Q_{663}\frac{\partial^3 w_s}{\partial x^2\partial y}\right) + \frac{K_0}{4}\left(\frac{\partial^4 v}{\partial x^4} - \frac{\partial^4 u}{\partial x^3\partial y} + \frac{\partial^4 v}{\partial x^2\partial y^2} - \frac{\partial^4 u}{\partial x\partial y^3}\right) = 0, \tag{26}$$

δw_b :

$$
\begin{aligned}
&Q_{222}\frac{\partial^4 w_b}{\partial y^4} - Q_{121}\frac{\partial^3 u}{\partial x\partial y^2} - Q_{221}\frac{\partial^3 v}{\partial y^3} + Q_{224}\frac{\partial^4 w_s}{\partial y^4} - Q_{237}\frac{\partial^2 \beta}{\partial y^2} - Q_{111}\frac{\partial^3 u}{\partial x^3} + Q_{112}\frac{\partial^4 w_b}{\partial x^4} - Q_{137}\frac{\partial^2 \beta}{\partial x^2} \\
&+Q_{114}\frac{\partial^4 w_s}{\partial x^4} - Q_{121}\frac{\partial^3 v}{\partial x^2\partial y} + 2\left(Q_{122}\frac{\partial^4 w_b}{\partial x^2\partial y^2} + Q_{124}\frac{\partial^4 w_s}{\partial x^2\partial y^2} - Q_{661}\frac{\partial^3 v}{\partial x^2\partial y} - Q_{661}\frac{\partial^3 u}{\partial y^2\partial x}\right) \\
&+4\left(Q_{662}\frac{\partial^4 w_b}{\partial x^2\partial y^2} + Q_{664}\frac{\partial^4 w_s}{\partial x^2\partial y^2}\right) + \frac{K_1}{2}\left(2\frac{\partial^4 \beta}{\partial x^2\partial y^2} + \frac{\partial^4 \beta}{\partial y^4} + \frac{\partial^4 \beta}{\partial x^4}\right) + \frac{K_2}{2}\left(\frac{\partial^4 w_s}{\partial y^4} + \frac{\partial^4 w_s}{\partial x^4} - 2\frac{\partial^4 w_s}{\partial x^2\partial y^2}\right) \\
&+\frac{K_0}{2}\left(2\frac{\partial^4 w_b}{\partial y^4} + 4\frac{\partial^4 w_b}{\partial x^2\partial y^2} + 2\frac{\partial^4 w_s}{\partial x^2\partial y^2} + 2\frac{\partial^4 w_b}{\partial y^4} + \frac{\partial^4 w_s}{\partial x^4} + \frac{\partial^4 w_s}{\partial y^4}\right) - K_w(w_s + w_b + \beta) \\
&+K_p\left(\frac{\partial^2 w_s}{\partial x^2} + \frac{\partial^2 w_b}{\partial x^2} + \frac{\partial^2 w_s}{\partial y^2} + \frac{\partial^2 w_b}{\partial y^2} + \frac{\partial^2 \beta}{\partial x^2} + \frac{\partial^2 \beta}{\partial y^2}\right) - (N_x^T + N_x^M)\left(\frac{\partial^2 w_s}{\partial x^2} + \frac{\partial^2 w_b}{\partial x^2}\right) \\
&-(N_y^T + N_y^M)\left(\frac{\partial^2 w_s}{\partial y^2} + \frac{\partial^2 w_b}{\partial y^2}\right) = 0,
\end{aligned}
\tag{27}
$$

δw_s :

$$
\begin{aligned}
&Q_{114}\frac{\partial^4 w_b}{\partial x^4} - Q_{113}\frac{\partial^3 u}{\partial x^3} - Q_{123}\frac{\partial^3 v}{\partial x^2\partial y} - Q_{123}\frac{\partial^3 u}{\partial y^2\partial x} + Q_{115}\frac{\partial^4 w_s}{\partial x^4} - Q_{223}\frac{\partial^3 v}{\partial y^3} + Q_{224}\frac{\partial^4 w_b}{\partial y^4} + Q_{225}\frac{\partial^4 w_s}{\partial y^4} \\
&-Q_{138}\frac{\partial^2 \beta}{\partial x^2} - Q_{4410}\frac{\partial^2 w_s}{\partial y^2} - Q_{238}\frac{\partial^2 \beta}{\partial y^2} - Q_{5510}\frac{\partial^2 w_s}{\partial x^2} + 4\left(Q_{664}\frac{\partial^4 w_b}{\partial x^2\partial y^2} + Q_{665}\frac{\partial^4 w_s}{\partial x^2\partial y^2}\right) \\
&+\frac{K_4}{4}\left(2\frac{\partial^4 \beta}{\partial x^2\partial y^2} + \frac{\partial^4 \beta}{\partial x^4} + \frac{\partial^4 \beta}{\partial y^4}\right) + 2\left(Q_{124}\frac{\partial^4 w_b}{\partial x^2\partial y^2} - Q_{663}\frac{\partial^3 v}{\partial x^2\partial y} + Q_{125}\frac{\partial^4 w_s}{\partial x^2\partial y^2} - Q_{663}\frac{\partial^3 u}{\partial x\partial y^2}\right) \\
&+\frac{K_0}{4}\left(4\frac{\partial^4 w_b}{\partial x^2\partial y^2} + 2\frac{\partial^4 w_b}{\partial y^4} + 2\frac{\partial^4 w_b}{\partial x^4} + 2\frac{\partial^4 w_s}{\partial x^2\partial y^2} + \frac{\partial^4 w_s}{\partial x^4} + \frac{\partial^4 w_s}{\partial y^4}\right) \\
&+\frac{K_1}{4}\left(2\frac{\partial^4 \beta}{\partial x^2\partial y^2} + \frac{\partial^4 \beta}{\partial x^4} + \frac{\partial^4 \beta}{\partial y^4}\right) - \frac{K_6}{4}\left(\frac{\partial^2 w_s}{\partial x^2} + \frac{\partial^2 w_s}{\partial y^2}\right) - \frac{K_7}{4}\left(\frac{\partial^2 \beta}{\partial x^2} + \frac{\partial^2 \beta}{\partial y^2}\right) \\
&+\frac{K_2}{2}\left(2\frac{\partial^4 w_b}{\partial y^2\partial x^2} + 2\frac{\partial^4 w_s}{\partial y^2\partial x^2} + \frac{\partial^4 w_b}{\partial y^4} + \frac{\partial^4 w_b}{\partial x^4} + \frac{\partial^4 w_s}{\partial y^4} + \frac{\partial^4 w_s}{\partial x^4}\right) \\
&+\frac{K_5}{4}\left(\frac{\partial^4 w_s}{\partial y^4} + \frac{\partial^4 w_s}{\partial x^4} + 2\frac{\partial^4 w_s}{\partial x^2\partial y^2}\right) - K_w(w_s + w_b + \beta) \\
&+K_p\left(\frac{\partial^2 w_s}{\partial x^2} + \frac{\partial^2 w_b}{\partial x^2} + \frac{\partial^2 w_s}{\partial y^2} + \frac{\partial^2 w_b}{\partial y^2} + \frac{\partial^2 \beta}{\partial x^2} + \frac{\partial^2 \beta}{\partial y^2}\right) - (N_x^T + N_x^M)\left(\frac{\partial^2 w_s}{\partial x^2} + \frac{\partial^2 w_b}{\partial x^2}\right) \\
&-(N_y^T + N_y^M)\left(\frac{\partial^2 w_s}{\partial y^2} + \frac{\partial^2 w_b}{\partial y^2}\right) = 0,
\end{aligned}
\tag{28}
$$

$\delta\beta$:

$$
\begin{aligned}
&Q_{136}\frac{\partial u}{\partial x}-Q_{5510}\frac{\partial^2 w_s}{\partial x^2}-Q_{138}\frac{\partial^2 w_s}{\partial x^2}+Q_{339}\beta+Q_{236}\frac{\partial v}{\partial y}-Q_{137}\frac{\partial^2 w_b}{\partial x^2}-Q_{4410}\frac{\partial^2 w_s}{\partial y^2}-Q_{237}\frac{\partial^2 w_b}{\partial y^2}\\
&-Q_{238}\frac{\partial^2 w_s}{\partial y^2}-\frac{K_7}{4}\left(\frac{\partial^2 w_s}{\partial x^2}+\frac{\partial^2 w_s}{\partial y^2}\right)+\frac{K_1}{4}\left(4\frac{\partial^4 w_b}{\partial x^2\partial y^2}+2\frac{\partial^4 w_b}{\partial x^4}+\frac{\partial^4 w_s}{\partial x^4}+2\frac{\partial^4 w_s}{\partial y^2\partial x^2}+2\frac{\partial^4 w_b}{\partial y^4}+\frac{\partial^4 w_s}{\partial y^4}\right)\\
&+\frac{K_3}{4}\left(\frac{\partial^4\beta}{\partial x^4}+\frac{\partial^4\beta}{\partial y^4}+2\frac{\partial^4\beta}{\partial y^2\partial x^2}\right)+\frac{K_4}{4}\left(\frac{\partial^4 w_s}{\partial y^4}+\frac{\partial^4 w_s}{\partial x^4}+2\frac{\partial^4 w_s}{\partial y^2\partial x^2}\right)-\frac{K_9}{4}\left(\frac{\partial^2\beta}{\partial y^2}+\frac{\partial^2\beta}{\partial x^2}\right)\\
&-K_w(w_s+w_b+\beta)+K_p\left(\frac{\partial^2 w_s}{\partial x^2}+\frac{\partial^2 w_b}{\partial x^2}+\frac{\partial^2 w_s}{\partial y^2}+\frac{\partial^2 w_b}{\partial y^2}+\frac{\partial^2\beta}{\partial x^2}+\frac{\partial^2\beta}{\partial y^2}\right)=0
\end{aligned}
\tag{29}
$$

4. Exact solution method

The differential equations are solved using a Navier type solution, such that the geometrical boundary conditions of the simply supported structure are fulfilled by the following displacement approximation [68]:

$$
\left\{\begin{array}{c} u(x,y)\\ v(x,y)\\ w_b(x,y),w_s(x,y),\beta(x,y)\end{array}\right\}=\sum_{m=1}^{\infty}\sum_{n=1}^{\infty}\left\{\begin{array}{c} U\cos(H_1x)\sin(H_2y)\\ V\cos(H_2y)\sin(H_1x)\\ (W_b,W_s,B)\sin(H_1x)\sin(H_2y)\end{array}\right\}
\tag{30}
$$

where H_1 and H_2 are defined as

$$
\mathrm{H}_1=\frac{m\pi}{a},\mathrm{H}_2=\frac{n\pi}{b}
\tag{31}
$$

and m and n refer to the mode number along the length and width directions, respectively. The unknown coefficients U, V, W_b, W_s, and B are then determined by solving the following matrix equation

$$
\left([K]_{5\times5}-P_{cr}[K_g]_{5\times5}\right)[U\quad V\quad W_b\quad W_s\quad \mathrm{B}]^t=[0]_{5\times1}
\tag{32}
$$

in which $[K]$ and $[K_g]$ are the stiffness and geometric stiffness matrices, respectively, P_{cr} also denotes the CBL. The CBLs of the microstructure are then determined by solving the classical eigenvalue problem represented by Eq. (32).

5. Results and discussions

In this section we perform a numerical assessment of the elastic buckling behavior for a three-layered sandwich microplate with a metal foam core and composite face sheets which are reinforced with GNPs. The proposed method is, first, validated by a comparative evaluation of our results with predictions available from literature [69], in terms of NCBLs for a simply supported square homogenous microplate, in absence of any elastic substrate of thermal environment, whose results are summarized in Table 1. Accordingly to Ref. [69], the following material properties are selected: $E = 14.4\times10^9$ Pa, $\nu = 0.38$, and $h = 17.6$ μm, and the NCBL is defined as $P^*_{cr} = P_{cr}a^2/Eh^3$. The NCBLs are obtained systematically for different aspect ratios and material length-scale parameter values in both uniaxial and biaxial loading types. Based on Table 1, it is worth observing that as the aspect ratio of the microstructure increases, the difference between the reference results [69] and the current work gradually reduces. Differently from Ref. [69], where a first-order shear deformation theory is applied neglecting the transverse normal strain component, in this study we propose a Q-3D S-N theory to improve the accuracy of the formulation and solution.

The metal foam core is composed of SUS304 with $E = 201.04\times10^9$ Pa, $\nu = 0.3262$, and $\alpha = 12.33\times10^{-6}$ K^{-1} [70], while the face sheets mentioned before, are reinforced with GNPs. GNPs specifications are: $E = 1.01\times10^{12}$ Pa, $\nu = 0.186$, $\alpha = 2.35\times10^{-5}$ K^{-1}, $l_{GNPs} = 2.5$ μm, $w_{GNPs} = 1.5$ μm, and $h_{GNPs} = 1.5$ nm [30]; and the face sheets' matrix properties are: $E = 130\times10^9$ Pa, $\nu = 0.34$, and $\alpha = 17\times10^{-6}$ K^{-1}. Besides, the following numerical values are considered for obtaining further results: $h = 17.6$ μm, $l = 0.6\ h$, $h_c = 0.8\ h$, $h_t = h_b = 0.1\ h$, $a = 10\ h$, $b = a/2$, $\gamma = 0.3$, g^*_{GNPs}=0.5 %, U-U pattern for the faces, Type B of imperfection for the core, and bi-axial loading type. Also, the NCBL is computed as $P^*_{cr} = P_{cr}/Ea$.

As first outcome, the effects of GNPs' weight fraction and also their different dispersion patterns on the NCBLs are investigated in Fig. 2. As can be seen from this figure, increasing the GNPs' weight fraction, even by a small amount up to one percent, the NCBLs increases significantly. As stated earlier, GNPs are one of the strongest materials known, with a tensile strength many times higher than that of steel. By adding GNPs to the composite, the overall strength of the material increases without adding much weight, resulting in a higher strength-to-weight ratio for the structure. Thus, the CBLs will enhance. Also, from Fig. 2 it can be found that the dispersion pattern of GNPs also plays an important role on their effectiveness in reinforcing the structures. It can be observed that for the FG V-A pattern, the NCBLs assume their maximum value, while reaching their minimum value for a FG A-V distribution. For the other patterns, the results are close together. Therefore, it is essential to control the dispersion of GNPs during the manufacturing process to optimize the CBLs and other mechanical properties of the composite material. Fig. 3 also shows that an increased imperfection ratio of the microstructure can lead to a reduction in the NCBLs. Porosity refers to the presence of voids or empty spaces within the material, and it can have a significant effect on the mechanical behavior of the structure, with an expected reduction of the cross-sectional area and load-carrying capacity, making the structure more susceptible to buckling under a compressive load. Also, the presence of voids weakens the material and reduces its overall stiffness and strength. In a solid structure, indeed, the atomic or molecular bonds provide the necessary strength to resist deformation and buckling. An increased porosity increases weakens bonds and interactions between the solid portions of the material, resulting in a decreased load-bearing capacity. Moreover, based on Fig. 2 it is worth observing that an increased temperature leads to a reduction in the NCBLs of the microstructure due to the phenomenon of thermal expansion and softening of materials. In this study, the effect of temperature on the thermal expansion coefficient is neglected. On the other hand, many materials, especially metals and polymers, tend to soften at elevated temperatures. Softening reduces the modulus of elasticity (i.e., stiffness) of the material, making it more susceptible to deformation under load. As the temperature increases, the material resistance to buckling decreases, leading to reduced CBLs. Note also that the effect of temperature variations for this microstructure is not significant as much as porosity variations. Fig. 4 shows that the type of

Table 1
Comparative evaluation of the NCBLs of the current study with ref. [69] in simple conditions.

Loading Type	Ref.	l/h	a/h 5	10	20
Uni-Axial	**Thai and Choi** [64] **($\varepsilon_{zz}=0$)**	**0**	30.6456	36.1492	37.8485
		0.2	35.2300	41.5214	43.4774
		0.4	48.5799	57.4956	60.3249
		0.6	69.5711	83.6543	88.2739
		0.8	96.5829	119.3314	127.1312
		1.0	127.7826	163.6539	176.6313
	Current Study ($\varepsilon_{zz}\neq 0$)	**0**	32.1172	36.7719	38.1610
		0.2	37.4859	42.4011	43.8592
		0.4	53.5981	59.2893	60.9538
		0.6	80.4622	87.4374	89.4451
		0.8	118.0812	126.8460	129.3329
		1.0	166.4550	177.5149	180.6174
Bi-Axial	**Thai and Choi** [64] **($\varepsilon_{zz}=0$)**	**0**	15.3228	18.0746	18.9243
		0.2	17.6150	20.7607	21.7387
		0.4	24.2899	28.7478	30.1625
		0.6	34.7856	41.8271	44.1369
		0.8	48.2915	59.6657	63.5656
		1.0	63.8913	81.8269	90.0574
	Current Study ($\varepsilon_{zz}\neq 0$)	**0**	16.0586	18.3860	19.0805
		0.2	18.7430	21.2006	21.9296
		0.4	26.7990	29.6446	30.4769
		0.6	40.2311	43.7187	44.7225
		0.8	59.0406	63.4230	64.6665
		1.0	83.2275	88.7574	90.3087

imperfection significantly affects the NCBLs of the microplate. A uniform type (here labeled as Type A) leads to lower values of NCBLs, while Types B and C which are related to symmetric and non-symmetric types of imperfection, respectively lead to higher NCBLs and the maximum values are for Type B. Consequently, engineers must carefully consider the type and distribution of imperfection when designing structures to ensure optimal performance and buckling resistance. In most cases, the minimization of porosity is essential to maintain the structural integrity and to improve the CBLs of the structure. Fig. 4 confirms the earlier findings about the effect of the imperfection ratio on the NCBLs. Fig. 5 depicts that the inclusion of the material length-scale parameter of MCST, *l*, can lead to an enhancement of NCBLs. At small length scales, microstructural features can introduce an additional resistance to buckling and can stabilize the structure against a premature failure. Also, an increased GNPs' weight fraction leads to an enhanced NCBL. In Tables 2-4, the effect of the imperfection ratio, GNPs' weight fraction, and loading type (uni-axial and bi-axial) on the exact values of NCBLs for

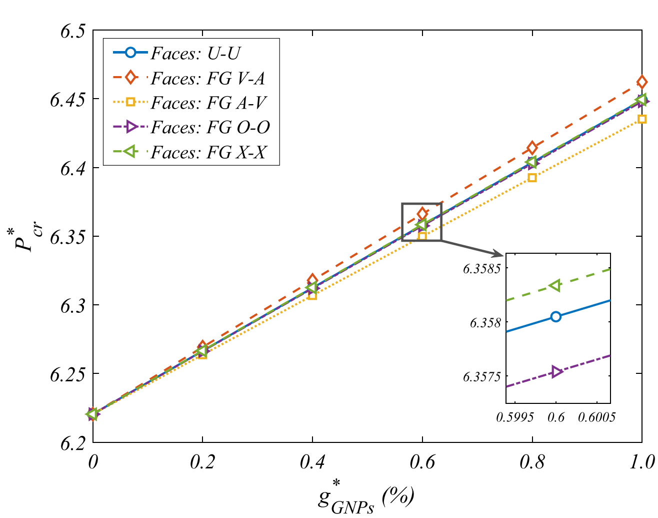

Fig. 2. Effect of the GNPs weight fraction percentage and their different types of dispersion on the NCBL.

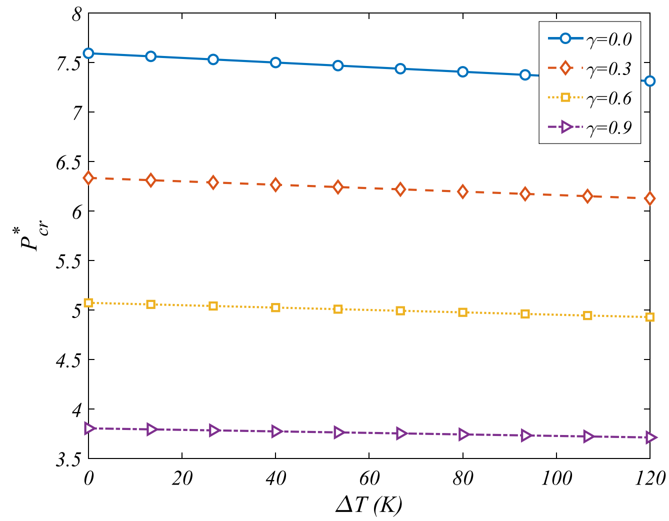

Fig. 3. Temperature changes and imperfection ratio impact on the NCBL.

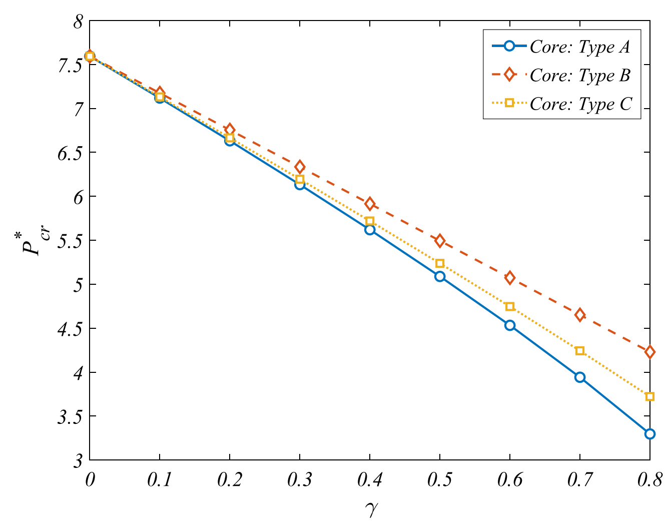

Fig. 4. Effect of different imperfection types and ratio on the NCBL.

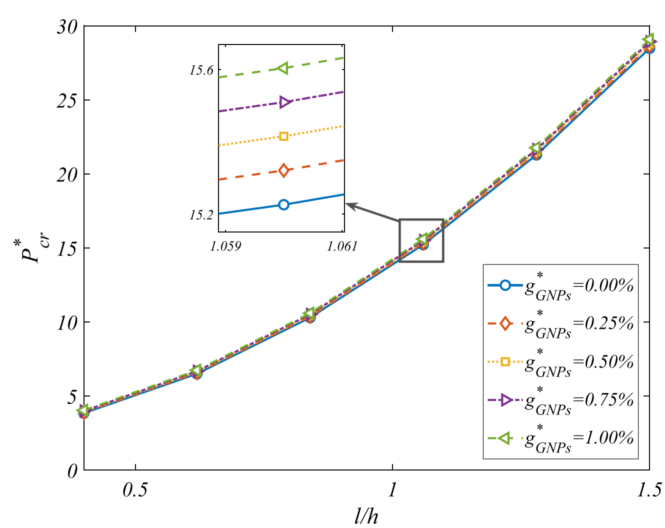

Fig. 5. Influence of the dimensionless material length-scale parameter and nano-fillers' weight fraction on the results.

Table 2
NCBLs based on a MCST and CET for various imperfection ratios and weight fractions of GNPs for a Type A imperfection model.

Loading Type	Theory	γ	g^*_{GNPs}(%) 0.0	0.5	1.0
Uni-Axial	MCST	0.00	37.3920	37.9703	38.5438
		0.25	31.3427	31.9204	32.4929
		0.50	24.8658	25.4427	26.0137
		0.75	17.5629	18.1380	18.7063
	CET	0.00	10.9929	11.4189	11.8393
		0.25	9.2399	9.6652	10.0843
		0.50	7.3628	7.7871	8.2043
		0.75	5.2463	5.6684	6.0820
Bi-Axial	MCST	0.00	7.4784	7.5941	7.7088
		0.25	6.2685	6.3841	6.4986
		0.50	4.9732	5.0885	5.2027
		0.75	3.5126	3.6276	3.7413
	CET	0.00	2.1986	2.2838	2.3679
		0.25	1.8480	1.9330	2.0169
		0.50	1.4726	1.5574	1.6409
		0.75	1.0493	1.1337	1.2164

imperfection Type A, B, and C is seen, respectively. According to these table, we can notice that an increased imperfection ratio reduces the NCBLs, which in turn increase for an increased GNPs' weight fraction. In addition, the results predicted by MCST and CET are compared in these

Table 3
NCBLs based on a MCST and CET for various imperfection ratios and weight fractions of GNPs for a Type B imperfection model.

Loading Type	Theory	γ	g^*_{GNPs}(%) 0.0	0.5	1.0
Uni-Axial	MCST	0.00	37.3920	37.9703	38.5438
		0.25	32.1514	32.7259	33.2955
		0.50	26.9030	27.4725	28.0371
		0.75	21.6406	22.2033	22.7611
	CET	0.00	10.9929	11.4189	11.8393
		0.25	9.9282	10.3467	10.7592
		0.50	8.8296	9.2366	9.6369
		0.75	7.6544	8.0408	8.4197
Bi-Axial	MCST	0.00	7.4784	7.5941	7.7088
		0.25	6.4303	6.5452	6.6591
		0.50	5.3806	5.4945	5.6074
		0.75	4.3281	4.4407	4.5522
	CET	0.00	2.1986	2.2838	2.3679
		0.25	1.9856	2.0693	2.1518
		0.50	1.7659	1.8473	1.9274
		0.75	1.5309	1.6082	1.6839

Table 4
NCBLs based on a MCST and CET for various imperfection ratios and weight fractions of GNPs for a Type C imperfection model.

Loading Type	Theory	γ	g^*_{GNPs}(%) 0.0	0.5	1.0
Uni-Axial	MCST	0.00	37.3920	37.9703	38.5438
		0.25	31.5761	32.1547	32.7280
		0.50	25.6027	26.1869	26.7647
		0.75	19.3187	19.9257	20.5229
	CET	0.00	10.9929	11.4189	11.8393
		0.25	9.3600	9.7856	10.2050
		0.50	7.5603	7.9910	8.4141
		0.75	5.4326	5.8868	6.3295
Bi-Axial	MCST	0.00	7.4784	7.5941	7.7088
		0.25	6.3152	6.4309	6.5456
		0.50	5.1205	5.2374	5.3529
		0.75	3.8637	3.9851	4.1046
	CET	0.00	2.1986	2.2838	2.3679
		0.25	1.8720	1.9571	2.0410
		0.50	1.5121	1.5982	1.6828
		0.75	1.0865	1.1774	1.2659

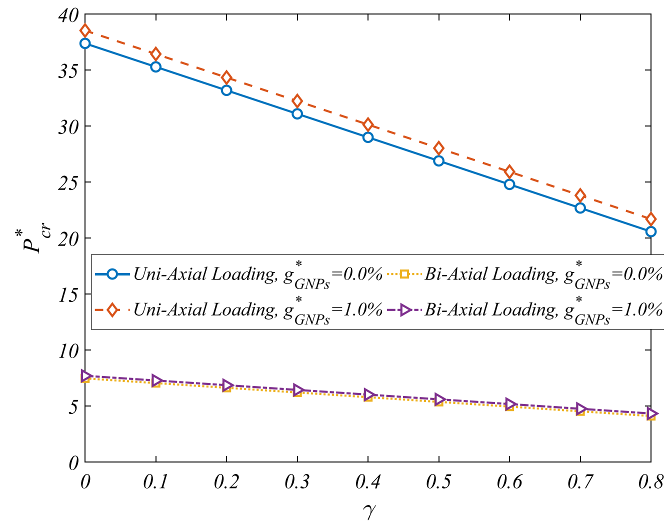

Fig. 6. Comparative evaluation of results for two loading cinditions: Uni-axial Vs. Bi-axial loadings.

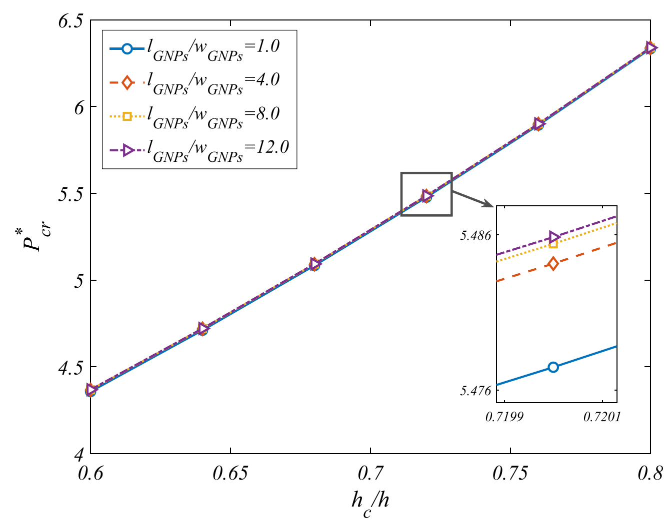

Fig. 7. Impact of the GNPs' length-to-width and the layers thickness ratios on the NCBL.

tables, where results obtained from MCST are higher than CET due to presence of the small-scale effect. Based on a comparative evaluation of these tables, the lowest values of results are associated to a Type A imperfection, whereas the highest values stem from a Type B imperfection. Fig. 6 also discusses about the influence of a uniaxial and biaxial loading condition on the elastic buckling behavior of the microplate. In the uniaxial loading case, the applied load is directed along a single axis, which allows the structure to withstand the applied load more efficiently. The entire cross-sectional area of the structure contributes to resist the load, leading to a higher CBL compared to a bi-axial loading, where the load is applied along two axes, and the structure may have less capacity to resist the combined loading condition. In Fig. 7, it is visible that an increased GNPs length-to-width ratio enhances the NCBLs. In fact, as the length-to-width ratio of GNPs increases, the platelets increase their axial deformability. with an increased effective surface area, and interfacial surface with the surrounding matrix material. This enhanced interfacial bonding increases the load transfer efficiency, leading to better reinforcement of the composite. As a result, higher aspect ratios generally lead to increased CBLs. The optimal length-to-width ratio of GNPs depends on the selected application, as well as on the mechanical properties of the matrix material, but also on the desired mechanical

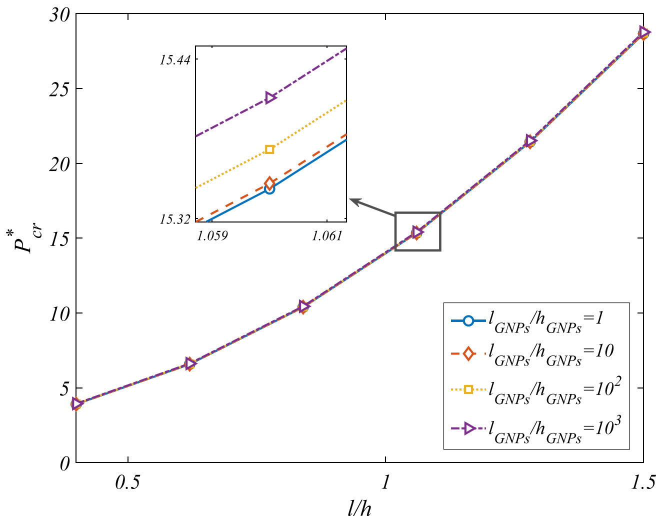

Fig. 8. Effect of the length-to-height of GNPs reinforcement on the NCBL.

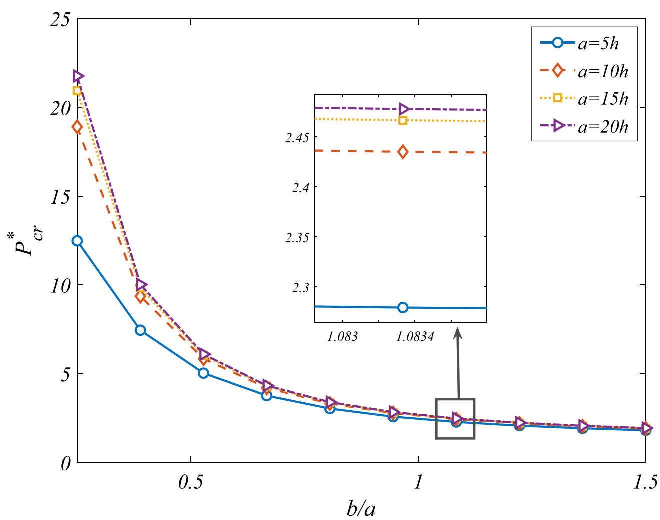

Fig. 9. Effect of the geometrical parameters variations on the results.

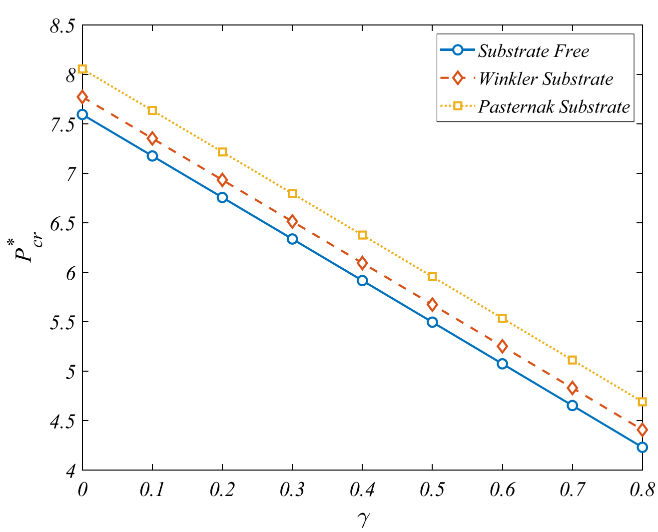

Fig. 10. Effect of different substrate conditions on the results.

behavior of the composite structure. Fig. 7 also shows the effect of the core-to-total thickness ratio whose increase leads the NCBLs to enhance due to an increased microstructural stiffness. According to Fig. 8, an increased GNPs length-to-height ratio leads an overall enhancement of the NCBLs. In fact, higher length-to-height ratios of GNPs often lead to a higher aspect ratio, where the platelets improve their axial deformability. This enhanced aspect ratio increases the reinforcement efficiency of the GNPs in the composite. Longer platelets have a larger effective interfacial surface with the surrounding matrix material. This improved interfacial bonding increases the load transfer efficiency and can lead to a better reinforcement, resulting in increased CBLs. Fig. 9 shows the impact of the microplate geometrical parameters on the NCBLs. The width-to-length ratio of the microplate is also related to its aspect ratio, defining the width-to-thickness rational value of the plate. For thin plates with a relatively constant thickness, the width-to-length ratio can be related to the aspect ratio. Higher aspect ratios (longer and narrower microplates) tend to feature higher CBLs compared to lower aspect ratios (shorter and wider microplates). Fig. 10 also compares the effect of different elastic substrate models on the NCBLs. In such a context, the Winkler and Pasternak models are commonly used to represent the behavior of elastic substrates or foundations when analyzing the buckling of structures resting on these supports. These models account for the interaction between the structure and the surrounding elastic medium, which can significantly influence the CBLs. The Winkler model typically enables lower CBLs compared to the Pasternak model. More specifically, the Winkler model just includes springs, whereas the inclusion of a shear layer in the Pasternak model provides an additional lateral support to the structure. This lateral support reduces the lateral deflections and lateral instability of the structure, leading to higher CBLs compared to the Winkler model. Thus, the choice of the elastic substrate model can significantly influence the CBLs of structures resting on elastic substrates, as shown in the last figure.

6. Conclusions

The present work has focused on the buckling behavior of metal foam microplates covered by GNPs- reinforced faces, as useful for many wearable sensors and sustainable construction materials, accounting for a gradual variation of the thermo-mechanical properties for each layer in the thickness direction. A novel Q-3D S-N hyperbolic theory has been used to define the kinematic relations of the microstructure, combined to a size-dependent MCST, whose governing equations of the problem are solved analytically to determine the microplate CBLs. A comparative evaluation of our results with predictions from literature ensures the correctness of the proposed theory, while assessing the impact of different input parameters on the NCBLs. Based on a parametric investigation, the following results can be summarized as follows:

- An increased quantity of GNPs as reinforcement phase, enhances the structural stiffness with an increased value of NCBLs. Also, by comparing different patterns of GNPs dispersion in the thickness path of the faces, it is revealed that FG V-A and FG A-V patterns lead to the maximum and minimum values of NCBLs, respectively.

- An imperfection ratio reduces the NCBLs. The symmetric Type B pattern of imperfection yields the highest values of CBLs, while the uniform Type A pattern leads to the least ones.

- An enhanced material length-scale parameter of MCST leads to increased values of CBLs, that also increase for higher length-to-width and length-to-height ratios of GNPs.

- An increased temperature will soften the microplate, thus reducing the CBLs, whereas the presence of an elastic substrate enhances the results with higher values of CBLs for a Pasternak model rather than a Winkler model. Generally, the uniaxial loading type requires higher values to reach CBLs in comparison to the biaxial loading type.

- It is finally observed that MCST predicts higher values of CBLs compared to a classical elasticity theory.

CRediT authorship contribution statement

Saeid Zavari: Data curation, Formal analysis, Investigation, Writing – original draft. **Ali Kaveh:** Data curation, Formal analysis, Investigation, Writing – original draft. **Hossein Babaei:** Data curation, Formal analysis, Investigation, Writing – original draft. **Ehsan Arshid:** Data curation, Formal analysis, Investigation, Writing – original draft. **Rossana Dimitri:** Conceptualization, Data curation, Formal analysis, Investigation, Methodology, Supervision, Validation, Writing – review & editing. **Francesco Tornabene:** Conceptualization, Data curation, Formal analysis, Investigation, Methodology, Supervision, Validation, Writing – review & editing.

Declaration of Competing Interest

The authors declare that they have no known competing financial interests or personal relationships that could have appeared to influence the work reported in this paper.

Data availability

No data was used for the research described in the article.

Appendix

We here provide more details about coefficients from Eqs. (25)-(29)

$$\{Q_{110},\quad Q_{111},\quad Q_{112}\}=\int_{-h/2}^{+h/2}Q_{11}^{cf}\{1,\quad z,\quad z^2\}\mathrm{d}z,$$

$$\{Q_{120},\quad Q_{121},\quad Q_{122}\}=\int_{-h/2}^{+h/2}Q_{12}^{cf}\{1,\quad z,\quad z^2\}\mathrm{d}z,$$

$$\{Q_{130},\quad Q_{131},\quad Q_{132}\}=\int_{-h/2}^{+h/2}Q_{13}^{cf}\{1,\quad z,\quad z^2\}\mathrm{d}z,$$

$$\{Q_{230},\quad Q_{231},\quad Q_{232}\}=\int_{-h/2}^{+h/2}Q_{23}^{cf}\{1,\quad z,\quad z^2\}\mathrm{d}z,$$

$$\{Q_{ii0},\quad Q_{ii1},\quad Q_{ii2}\}=\int_{-h/2}^{+h/2}Q_{ii}^{cf}\{1,\quad z,\quad z^2\}\mathrm{d}z,(i=2,3,4,5,6)$$

$$\{Q_{113},\quad Q_{114},\quad Q_{115}\}=\int_{-h/2}^{+h/2}Q_{11}^{cf}f(z)\{1,\quad z,\quad f(z)\}\mathrm{d}z,$$

$$\{Q_{123},\quad Q_{124},\quad Q_{125}\}=\int_{-h/2}^{+h/2}Q_{12}^{cf}f(z)\{1,\quad z,\quad f(z)\}\mathrm{d}z,$$

$$\{Q_{133},\quad Q_{134},\quad Q_{135}\}=\int_{-h/2}^{+h/2}Q_{13}^{cf}f(z)\{1,\quad z,\quad f(z)\}\mathrm{d}z,$$

$$\{Q_{233},\quad Q_{234},\quad Q_{235}\}=\int_{-h/2}^{+h/2}Q_{23}^{cf}f(z)\{1,\quad z,\quad f(z)\}\mathrm{d}z,$$

$$\{Q_{ii3},\quad Q_{ii4},\quad Q_{ii5}\}=\int_{-h/2}^{+h/2}Q_{ii}^{cf}f(z)\{1,\quad z,\quad f(z)\}\mathrm{d}z,(i=2,3,4,5,6)$$

$$\{Q_{116},\quad Q_{117},\quad Q_{118}\}=\int_{-h/2}^{+h/2}Q_{11}^{cf}h'(z)\{1,\quad z,\quad f(z)\}\mathrm{d}z,$$

$$\{Q_{126},\quad Q_{127},\quad Q_{128}\}=\int_{-h/2}^{+h/2}Q_{12}^{cf}h'(z)\{1,\quad z,\quad f(z)\}\mathrm{d}z,$$

$$\{ Q_{136}, \quad Q_{137}, \quad Q_{138} \} = \int_{-h/2}^{+h/2} Q_{13}^{c,f} h'(z) \{ 1, \quad z, \quad f(z) \} \mathrm{d}z,$$

$$\{ Q_{236}, \quad Q_{237}, \quad Q_{238} \} = \int_{-h/2}^{+h/2} Q_{23}^{c,f} h'(z) \{ 1, \quad z, \quad f(z) \} \mathrm{d}z,$$

$$\{ Q_{ii6}, \quad Q_{ii7}, \quad Q_{ii8} \} = \int_{-h/2}^{+h/2} Q_{ii}^{c,f} h'(z) \{ 1, \quad z, \quad f(z) \} \mathrm{d}z, (i = 2, 3, 4, 5, 6)$$

$$\{ Q_{119}, \quad Q_{1110} \} = \int_{-h/2}^{+h/2} Q_{11}^{c,f} \{ (h'(z))^2, \quad h^2(z) \} \mathrm{d}z,$$

$$\{ Q_{129}, \quad Q_{1210} \} = \int_{-h/2}^{+h/2} Q_{12}^{c,f} \{ (h'(z))^2, \quad h^2(z) \} \mathrm{d}z,$$

$$\{ Q_{139}, \quad Q_{1310} \} = \int_{-h/2}^{+h/2} Q_{13}^{c,f} \{ (h'(z))^2, \quad h^2(z) \} \mathrm{d}z,$$

$$\{ Q_{239}, \quad Q_{2310} \} = \int_{-h/2}^{+h/2} Q_{23}^{c,f} \{ (h'(z))^2, \quad h^2(z) \} \mathrm{d}z,$$

$$\{ Q_{ii9}, \quad Q_{ii10} \} = \int_{-h/2}^{+h/2} Q_{ii}^{c,f} \{ (h'(z))^2, \quad h^2(z) \} \mathrm{d}z, (i = 2, 3, 4, 5, 6)$$

$$\{ K_0, \quad K_1, \quad K_2, K_3, \quad K_4 \} = \int_{-h/2}^{+h/2} l\mu(z) \{ h(z), \quad f^{'}(z), \quad h^2(z), h(z)f^{'}(z), \quad f'^2(z) \} \mathrm{d}z,$$

$$\{ K_5, \quad K_6, \quad K_7, K_8, \quad K_9 \} = \int_{-h/2}^{+h/2} l\mu(z) \{ f''^2(z), \quad h'(z)f^{'}(z), \quad f''(z), h'^2(z), \quad h'(z) \} \mathrm{d}z$$

References

[1] H. Hebali, L. Boulefrakh, A. Chikh, A.A. Bousahla, A. Tounsi, S.R. Mahmoud, The effect of parameters of visco-Pasternak foundation on the bending and vibration properties of a thick FG plate, Geomech. Eng. 18 (2019) 161–178. 10.12989/GAE.2019.18.2.161.

[2] F.M.V. Ebrahimi, Vibration analysis of magneto-flexo-electrically actuated porous rotary nanobeams considering thermal effects via nonlocal strain gradient elasticity theory, Adv. Nano Res. 7 (2019) 223–231. 10.12989/anr.2019.7.4.223.

[3] Zaoui FZ, Ouinas D, Tounsi A. New 2D and quasi-3D shear deformation theories for free vibration of functionally graded plates on elastic foundations. Compos Part B Eng 2019;159:231–47. https://doi.org/10.1016/J.COMPOSITESB.2018.09.051.

[4] Zavari S, Bakhshi-Jooybari M, Gorji H. Combined electrohydraulic and flexible pin die forming: a novel high strain rate forming die setup. Int J Adv Manuf Technol 2020;111:2171–87. https://doi.org/10.1007/s00170-020-06242-5.

[5] Wang YQ, Zhao HL, Ye C, Zu JW. A porous microbeam model for bending and vibration analysis based on the sinusoidal beam theory and modified strain gradient theory. Int J Appl Mech 2018;10. https://doi.org/10.1142/S175882511850059X.

[6] Gao W, Qin Z, Chu F. Wave propagation in functionally graded porous plates reinforced with graphene platelets. Aerosp Sci Technol 2020;102:105860. https://doi.org/10.1016/j.ast.2020.105860.

[7] Chen D, Kitipornchai S, Yang J. Nonlinear free vibration of shear deformable sandwich beam with a functionally graded porous core. Thin-Walled Struct 2016;107:39–48. https://doi.org/10.1016/j.tws.2016.05.025.

[8] Gao K, Gao W, Chen D, Yang J. Nonlinear free vibration of functionally graded graphene platelets reinforced porous nanocomposite plates resting on elastic foundation. Compos Struct 2018;204:831–46. https://doi.org/10.1016/j.compstruct.2018.08.013.

[9] Taati E, Fallah F, Ahmadian MT. Subsonic and supersonic flow-induced vibration of sandwich cylindrical shells with FG-CNT reinforced composite face sheets and metal foam core. Int J Mech Sci 2022;215:106918. https://doi.org/10.1016/J.IJMECSCI.2021.106918.

[10] Karimiasl M, Ebrahimi F, Akgöz B. Buckling and post-buckling responses of smart doubly curved composite shallow shells embedded in SMA fiber under hygro-thermal loading. Compos Struct 2019;223:110988. https://doi.org/10.1016/J.COMPSTRUCT.2019.110988.

[11] Sahmani S, Aghdam MM. Axial postbuckling analysis of multilayer functionally graded composite nanoplates reinforced with GPLs based on nonlocal strain gradient theory. Eur Phys J Plus 2017;132:490. https://doi.org/10.1140/EPJP/I2017-11773-4.

[12] Mosayyebi M, Ashenai Ghasemi F, Aghaee M. Modified couple stress theory for wave propagation in viscoelastic sandwich microplates with FG-GPLRC core and piezoelectric face sheets as sensor and actuator. Waves Random Complex Media 2022. https://doi.org/10.1080/17455030.2022.2106387.

[13] Yang Y, Chen B, Lin W, Li Y, Dong Y. Vibration and symmetric thermal buckling of asymmetric annular sandwich plates with piezoelectric/GPLRC layers rested on foundation. Aerosp Sci Technol 2021;110:106495. https://doi.org/10.1016/j.ast.2021.106495.

[14] B. Safaei, F.H. Khoda, A.M. Fattahi, Non-classical plate model for single-layered graphene sheet for axial buckling, Adv. Nano Res. 7 (2019) 265–275. 10.12989/anr.2019.7.4.265.

[15] Akgöz B, Civalek Ö. Vibrational characteristics of embedded microbeams lying on a two-parameter elastic foundation in thermal environment. Compos Part B Eng 2018;150:68–77. https://doi.org/10.1016/j.compositesb.2018.05.049.

[16] Huang X, Zhang Y, Moradi Z, Shafiei N. Computer simulation via a couple of homotopy perturbation methods and the generalized differential quadrature

method for nonlinear vibration of functionally graded non-uniform micro-tube. Eng Comput 2022;38:2481–98. https://doi.org/10.1007/s00366-021-01395-7.
[17] Ahmadi A, Ghassemi A. Investigation both actions of elastic foundation parameters and small scale effect on axisymmetric bending of annular single-layered graphene sheet resting on an elastic medium. Phys E Low-Dimensional Syst Nanostruct 2018;103:208–26. https://doi.org/10.1016/j.physe.2018.05.028.
[18] Liu S, Yu T, Van Lich L, Yin S, Bui TQ. Size and surface effects on mechanical behavior of thin nanoplates incorporating microstructures using isogeometric analysis. Comput Struct 2019;212:173–87. https://doi.org/10.1016/j.compstruc.2018.10.009.
[19] Jabbari M, Joubaneh EF, Khorshidvand AR, Eslami MR. Buckling analysis of porous circular plate with piezoelectric actuator layers under uniform radial compression. Int J Mech Sci 2013;70:50–6. https://doi.org/10.1016/J.IJMECSCI.2013.01.031.
[20] Mojahedin A, Jabbari M, Khorshidvand AR, Eslami MR. Buckling analysis of functionally graded circular plates made of saturated porous materials based on higher order shear deformation theory. Thin-Walled Struct 2016;99:83–90. https://doi.org/10.1016/j.tws.2015.11.008.
[21] Feyzi MR, Khorshidvand AR. Axisymmetric post-buckling behavior of saturated porous circular plates. Thin-Walled Struct 2017;112:149–58. https://doi.org/10.1016/J.TWS.2016.11.026.
[22] Dhuria M, Grover N, Goyal K. Influence of porosity distribution on static and buckling responses of porous functionally graded plates. Structures 2021;34:1458–74. https://doi.org/10.1016/j.istruc.2021.08.050.
[23] Van Vinh P, Van Chinh N, Tounsi A. Static bending and buckling analysis of bi-directional functionally graded porous plates using an improved first-order shear deformation theory and FEM. Eur J Mech - A/Solids 2022;96:104743. https://doi.org/10.1016/J.EUROMECHSOL.2022.104743.
[24] Barati MR. Porosity-dependent vibration and dynamic stability of compositionally gradient nanofilms using nonlocal strain gradient theory. Proc Inst Mech Eng Part C J Mech Eng Sci 232 2018:3144–55. https://doi.org/10.1177/0954406217729421.
[25] T.H.L. Bekkaye, B. Fahsi, A.A. Bousahla, F. Bourada, A. Tounsi, K.H. Benrahou, A. Tounsi, M.M. Al-Zahrani, Porosity-dependent mechanical behaviors of FG plate using refined trigonometric shear deformation theory, Comput. Concr. 26 (2020) 439–450. 10.12989/cac.2020.26.5.439.
[26] Pollien A, Conde Y, Pambaguian L, Mortensen A. Graded open-cell aluminium foam core sandwich beams. Mater Sci Eng A 2005;404:9–18. https://doi.org/10.1016/j.msea.2005.05.096.
[27] Zenkour AM, Aljadani MH. Porosity effect on thermal buckling behavior of actuated functionally graded piezoelectric nanoplates. Eur J Mech A/Solids 2019;78:103835. https://doi.org/10.1016/j.euromechsol.2019.103835.
[28] Banhart J. Manufacture, characterisation and application of cellular metals and metal foams. Prog Mater Sci 2001;46:559–632. https://doi.org/10.1016/S0079-6425(00)00002-5.
[29] P.S. Liu, G.F. Chen, Porous Materials: Processing and Applications, Elsevier Inc., 2014. 10.1016/C2012-0-03669-1.
[30] Arshid E, Amir S, Loghman A. Static and dynamic analyses of FG-GNPs reinforced porous nanocomposite annular micro-plates based on MSGT. Int J Mech Sci 2020;180:105656. https://doi.org/10.1016/j.ijmecsci.2020.105656.
[31] Cuong-Le T, Hoang-Le M, Ferreira AJM, Abdel Wahab M. Small size-effect isogeometric analysis for linear and nonlinear responses of porous metal foam microplate. Compos Struct 2022;285:115189. https://doi.org/10.1016/j.compstruct.2022.115189.
[32] Pham Q-H, Nguyen P-C. Dynamic stability analysis of porous functionally graded microplates using a refined isogeometric approach. Compos Struct 2022;284:115086. https://doi.org/10.1016/j.compstruct.2021.115086.
[33] Hung PT, Phung-Van P, Thai CH. A refined isogeometric plate analysis of porous metal foam microplates using modified strain gradient theory. Compos Struct 2022;289:115467. https://doi.org/10.1016/J.COMPSTRUCT.2022.115467.
[34] V.-T. Tran, T.-K. Nguyen, H. Nguyen-Xuan, M. Abdel Wahab, Vibration and buckling optimization of functionally graded porous microplates using BCMO-ANN algorithm, Thin-Walled Struct. 182 (2023) 110267. 10.1016/j.tws.2022.110267.
[35] B. Akgöz, Ö. Civalek, Longitudinal vibration analysis for microbars based on strain gradient elasticity theory, J. Vibr. Control. 20(4) 10.1177/1077546312463752.
[36] A.G. Arani, G.S. Jafari, Nonlinear vibration analysis of laminated composite Mindlin micro/nano-plates resting on orthotropic Pasternak medium using DQM, Appl. Math. Mech. (English Ed. 36 (2015) 1033–1044. 10.1007/s10483-015-1969-7.
[37] Akgöz B, Civalek Ö. A novel microstructure-dependent shear deformable beam model. Int J Mech Sci 2015;99:10–20. https://doi.org/10.1016/j.ijmecsci.2015.05.003.
[38] Akgöz B, Civalek Ö. Bending analysis of embedded carbon nanotubes resting on an elastic foundation using strain gradient theory. Acta Astronaut 2016;119:1–12. https://doi.org/10.1016/j.actaastro.2015.10.021.
[39] Liu S, Yu T, Bui TQ. Size effects of functionally graded moderately thick microplates: A novel non-classical simple-FSDT isogeometric analysis. Eur J Mech A/Solids 2017;66:446–58. https://doi.org/10.1016/j.euromechsol.2017.08.008.
[40] Liu S, Yu T, Van Lich L, Yin S, Bui TQ. Size effect on cracked functional composite micro-plates by an XIGA-based effective approach. Meccanica 2018;53:2637–58. https://doi.org/10.1007/s11012-018-0848-9.
[41] Mao JJ, Lu HM, Zhang W, Lai SK. Vibrations of graphene nanoplatelet reinforced functionally gradient piezoelectric composite microplate based on nonlocal theory. Compos Struct 2020;236:111813. https://doi.org/10.1016/J.COMPSTRUCT.2019.111813.
[42] Bacciocchi M, Tarantino AM. Analytical solutions for vibrations and buckling analysis of laminated composite nanoplates based on third-order theory and strain gradient approach. Compos Struct 2021;272. https://doi.org/10.1016/j.compstruct.2021.114083.
[43] Karamanli A. Transient vibration analysis of strain gradient multi-directional functionally graded microplates under a moving concentrated load. Compos Struct 2023;308. https://doi.org/10.1016/j.compstruct.2023.116678.
[44] Chen X, Shen H-S, Xiang Y. Re-examination of thermo-mechanical buckling and postbuckling responses of sandwich plates with porous FG-GPLRC core. Thin-Walled Struct 2023;187:110735. https://doi.org/10.1016/j.tws.2023.110735.
[45] Fang J, Yin B, Li L, Zhang D. Thermal buckling and vibration analysis of rotating porous FG GNPs-reinforced Reddy microplates. Aerosp Sci Technol 2023;137:108298. https://doi.org/10.1016/j.ast.2023.108298.
[46] Anamagh MR, Bediz B. Free vibration and buckling behavior of functionally graded porous plates reinforced by graphene platelets using spectral Chebyshev approach. Compos Struct 2020;253:112765. https://doi.org/10.1016/j.compstruct.2020.112765.
[47] Yaghoobi H, Taheri F. Analytical solution and statistical analysis of buckling capacity of sandwich plates with uniform and non-uniform porous core reinforced with graphene nanoplatelets. Compos Struct 2020;252:112700. https://doi.org/10.1016/j.compstruct.2020.112700.
[48] Kim J, Żur KK, Reddy JN. Bending, free vibration, and buckling of modified couples stress-based functionally graded porous micro-plates. Compos Struct 2019;209:879–88. https://doi.org/10.1016/j.compstruct.2018.11.023.
[49] Khorasani M, Soleimani-Javid Z, Arshid E, Lampani L, Civalek Ö. Thermo-elastic buckling of honeycomb micro plates integrated with FG-GNPs reinforced Epoxy skins with stretching effect. Compos Struct 2021;258:113430. https://doi.org/10.1016/j.compstruct.2020.113430.
[50] Lin HG, Cao DQ, Xu YQ. Vibration, buckling and aeroelastic analyses of functionally graded multilayer graphene-nanoplatelets-reinforced composite plates embedded in piezoelectric layers. Int J Appl Mech 2018;10. https://doi.org/10.1142/S1758825118500230.
[51] Shen HS, Xiang Y, Fan Y. Nonlinear vibration of functionally graded graphene-reinforced composite laminated cylindrical shells in thermal environments. Compos Struct 2017;182:447–56. https://doi.org/10.1016/j.compstruct.2017.09.010.
[52] Z.X. Lei, K.M. Liew, J.L. Yu, Free vibration analysis of functionally graded carbon nanotube-reinforced composite plates using the element-free kp-Ritz method in thermal environment, (2013). 10.1016/j.compstruct.2013.06.003.
[53] Allahkarami F, Nikkhah-Bahrami M. The effects of agglomerated CNTs as reinforcement on the size-dependent vibration of embedded curved microbeams based on modified couple stress theory. Mech Adv Mater Struct 2018;25:995–1008. https://doi.org/10.1080/15376494.2017.1323144.
[54] Moradi-Dastjerdi R, Behdinan K, Safaei B, Qin Z. Static performance of agglomerated CNT-reinforced porous plates bonded with piezoceramic faces. Int J Mech Sci 2020;188:105966. https://doi.org/10.1016/j.ijmecsci.2020.105966.
[55] Van Thanh N, Dinh Quang V, Dinh Khoa N, Seung-Eock K, Dinh Duc N. Nonlinear dynamic response and vibration of FG CNTRC shear deformable circular cylindrical shell with temperature-dependent material properties and surrounded on elastic foundations. J Sandw Struct Mater 2018;21:2456–83. https://doi.org/10.1177/1099636217752243.
[56] Shahsavari D, Shahsavari M, Li L, Karami B. A novel quasi-3D hyperbolic theory for free vibration of FG plates with porosities resting on Winkler/Pasternak/Kerr foundation. Aerosp Sci Technol 2018;72:134–49. https://doi.org/10.1016/j.ast.2017.11.004.
[57] Kiran MC, Kattimani SC. Assessment of porosity influence on vibration and static behaviour of functionally graded magneto-electro-elastic plate: A finite element study. Eur J Mech A/Solids 2018;71:258–77. https://doi.org/10.1016/j.euromechsol.2018.04.006.
[58] Zhao J, Xie F, Wang A, Shuai C, Tang J, Wang Q. Dynamics analysis of functionally graded porous (FGP) circular, annular and sector plates with general elastic restraints. Compos Part B Eng 2019;159:20–43. https://doi.org/10.1016/j.compositesb.2018.08.114.
[59] F. Ebrahimi, A. Jafari, V. Mahesh, Assessment of porosity influence on dynamic characteristics of smart heterogeneous magneto-electro-elastic plates, Struct. Eng. Mech. 72 (2019) 875–891. 10.12989/sem.2019.72.1.113.
[60] K. Jermsittiparsert, A. Ghabussi, A. Forooghi, A. Shavalipour, M. Habibi, D. won Jung, M. Safa, Critical voltage, thermal buckling and frequency characteristics of a thermally affected GPL reinforced composite microdisk covered with piezoelectric actuator, Mech. Based Des. Struct. Mach. (2020). 10.1080/15397734.2020.1748052.
[61] Karami B, Shahsavari D, Janghorban M, Tounsi A. Resonance behavior of functionally graded polymer composite nanoplates reinforced with graphene nanoplatelets. Int J Mech Sci 2019;156:94–105. https://doi.org/10.1016/j.ijmecsci.2019.03.036.
[62] Damercheloo AR, Khorshidvand AR, Khorsandijou SM, Jabbari M. Free vibrational characteristics of GNP-reinforced joined conical–conical shells with different boundary conditions. Thin-Walled Struct 2021;169:108287. https://doi.org/10.1016/J.TWS.2021.108287.
[63] Arshid E, Momeni Nia MJ, Ghorbani MA, Civalek Ö, Kumar A. On the poroelastic vibrations of lightweight FGSP doubly-curved shells integrated with GNPs-reinforced composite coatings in thermal atmospheres. Appl Math Model 2023;124:122–41. https://doi.org/10.1016/j.apm.2023.07.036.
[64] Zhang B, Li H, Kong L, Zhang X, Feng Z. Variational formulation and differential quadrature finite element for freely vibrating strain gradient Kirchhoff plates. ZAMM - J Appl Math Mech / Z Angew Math Und Mech 2021;101:e202000046.

[65] Karamanli A, Vo TP. Size-dependent behaviour of functionally graded sandwich microbeams based on the modified strain gradient theory. Compos Struct 2020;246:112401. https://doi.org/10.1016/j.compstruct.2020.112401.

[66] vibration analysis of FG saturated porous annular/ circular micro sandwich plates embedded with nano-composite face sheets subjected to multi-physical pre loads, Smart Struct. Syst. 23 (2019) 429–447. 10.12989/sss.2019.23.5.429.

[67] Natarajan S, Haboussi M, Manickam G. Application of higher-order structural theory to bending and free vibration analysis of sandwich plates with CNT reinforced composite facesheets. Compos Struct 2014;113:197–207. https://doi.org/10.1016/j.compstruct.2014.03.007.

[68] H. Matouk, A.A. Bousahla, H. Heireche, F. Bourada, E.A.A. Bedia, A. Tounsi, S.R. Mahmoud, A. Tounsi, K.H. Benrahou, Investigation on hygro-thermal vibration of P-FG and symmetric S-FG nanobeam using integral Timoshenko beam theory, Adv. Nano Res. 8 (2020) 293–305. 10.12989/anr.2020.8.4.293.

[69] Thai H-T, Choi D-H. Size-dependent functionally graded Kirchhoff and Mindlin plate models based on a modified couple stress theory. Compos Struct 2013;95:142–53. https://doi.org/10.1016/j.compstruct.2012.08.023.

[70] Bui TQ, Van Do T, Ton LHT, Doan DH, Tanaka S, Pham DT, et al. On the high temperature mechanical behaviors analysis of heated functionally graded plates using FEM and a new third-order shear deformation plate theory. Compos Part B Eng 2016;92:218–41. https://doi.org/10.1016/j.compositesb.2016.02.048.